https://doi.org/10.1063/5.0166526

Accepted to Phys. Fluids 10.1063/5.0166526



# Coexistence of natural and forced vortex dislocations in step cylinder flow

Cai Tian (田偲),[1, a)] Jianxun Zhu (朱建勋),[1] and Lars Erik Holmedal[1]
*Department of Marine Technology, Norwegian University of Science and Technology (NTNU), NO-7491 Trondheim, Norway*

(Dated: 11 August 2023)

The wake behind a step cylinder (consisting of a small diameter cylinder ($d$) and a large diameter cylinder ($D$)) with diameter ratio $D/d = 2$ at Reynolds number $Re_D$=200 (the mode A$^*$ regime) is simulated by direct numerical simulations. New detailed information of the interaction between natural vortex dislocations and forced vortex dislocations is described. In the large cylinder wake, the forced and natural vortex dislocations coexist. The regular formation of forced vortex dislocation is found to be delayed under the effect of natural vortex dislocations. The occurrence of natural vortex dislocations is suppressed in the large cylinder wake close to the small cylinder. Moreover, the effect of vortex dislocations on structural loads are described. The results in this paper provide a more thorough understanding of the formation and interaction between the natural and forced vortex dislocations.

[a)]Author to whom correspondence should be addressed. Electronic mail: cai.tian@ntnu.no

Accepted to Phys. Fluids 10.1063/5.0166526



## I. INTRODUCTION

As a fundamental transition feature in cylindrical structural wakes, vortex dislocations are usually referred to as the flow region where the neighboring spanwise vortices move out of phase due to different shedding frequencies[1]. There are mainly two types of vortex dislocations: Natural vortex dislocation (NVD) and forced vortex dislocation (FVD).

Natural vortex dislocations form naturally when bluff-body wakes exhibit three-dimensional transitions. For example, the wake behind a circular cylinder becomes three-dimensional when the Reynolds number ($Re_D = UD/\nu$ where $U$ represents the uniform inflow velocity, $D$ is the cylinder diameter, and $\nu$ is the kinematic viscosity of the fluid) exceeds around 190, due to the mode A instability, originating from the elliptic instability[2]. A stable state of mode A occurs first at 190$< Re <$193[2,3] and is characterized by two counter-rotating streamwise vortices forming a mode A vortex loop with a spanwise wavelength around $4D$. At 193$< Re <$230, this flow becomes unstable and is denoted mode A$^*$. Here an intermittent large-scale vortex dislocation (also called the spot-like vortex dislocation[4]) occurs randomly in the wake both in time and over the spanwise position[2,5–7]. As $Re$ further increases to above 230, the wake flow transforms to mode B[2,8] and further on towards turbulence[9,10] where the natural vortex dislocation still exists but with a decreased probability and duration of occurrence[10].

Forced vortex dislocations occurs in the wake behind a nonuniform geometry, such as step cylinders[12,13], ring-attached cylinders[4], and cylinders with end effects[1,14,15]. In most of these cases, several spanwise vortices occur in the wake due to the spanwise disturbance induced by the geometrical non-uniformity. Due to the different resulting shedding frequencies, the phase difference between two neighboring vortex cells will continuously accumulate, yielding the forced vortex dislocations. This process occurs regularly at a beat frequency ($f_{beat} = f_1$-$f_2$) between the frequencies of the two neighboring vortices (where $f_1$ and $f_2$ represent the vortex with the higher and lower shedding frequency, respectively). Detailed investigations[5,7,16,17] of the near wake show that both natural and forced vortex dislocation induce a decrease in the vortex shedding frequency, an increase in the base pressure, and an increase in the fluctuation amplitude of spanwise flow in the surrounding flow region.

The step cylinder sketched in figure 1(a) is convenient for investigating vortex dislocations due to its simple geometry and multiple spanwise vortices in the wake. For a step cylinder with $D/d > 1.55$ at 63<$Re_D$<3900, three dominating spanwise vortices have been observed in the wake

Accepted to Phys. Fluids 10.1063/5.0166526



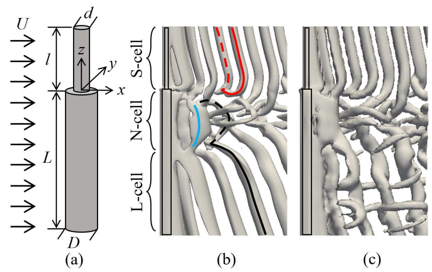


FIG. 1. (a) A sketch of the step cylinder geometry. The diameters of the small and large cylinders are $d$ and $D$, respectively. $l$ is the length of the small cylinder, and $L$ is the length of the large cylinder. The origin locates at the center of the interface between the small and large cylinders. The uniform incoming flow $U$ is in the positive $x-$direction. The three directions are named streamwise ($x-$direction), crossflow ($y-$direction), and spanwise ($z-$direction). (b) The isosurfaces of $\lambda_2 = -0.05$[18] shows the instantaneous wake behind a step cylinder with $D/d = 2$ at $Re_D = 150$ from Tian et al.[13], taken at the moment when vortex dislocations occur. The SS-half loop and NL-loop structures are denoted by the red and black curves, where the solid and dashed curves represent the vortex shed from the -Y and +Y sides of the step cylinder, respectively. (c) The isosurfaces of $\lambda_2 = -0.05$ shows the instantaneous wake behind a step cylinder with $D/d = 2$ at $Re_D = 200$ from the present study.

in previous studies[12,13,19–21]: (i) The S-cell vortex behind the small cylinder with the highest shedding frequency $f_S$, (ii) the L-cell vortex sheds from the large cylinder with the lower shedding frequency $f_L$, and (iii) the N-cell vortex located between the S- and L-cell vortices with the lowest shedding frequency $f_N$. The forced vortex dislocation (FVD) occurs periodically between neighboring vortex cells. When FVD occurs between the S- and N-cell vortices, the connection between the corresponding S- and N-cell vortices is broken; two S-cell vortices with opposite rotating directions connect (i.e., the S-S half loop vortex structure forms[19,20], as denoted by the red curve in figure 1(b)). When FVD starts to occur between the N- and L-cell vortices, one L-cell vortex (e.g., the one denoted by the solid black curve in figure 1(b)) dislocates with its corresponding N-cell vortex (as denoted by the blue solid curve in figure 1(b)) and connects to the N-cell vortex on the other side of the step cylinder (as denoted by the black dashed curve in figure 1(b)), forming the NL-loop structure. These NL vortex loops will be focused on in the present paper as they indicating the formation of vortex dislocations between the N- and L-cell vortices. As FVD occurs, a series of NL-loop structures, NN-loop structure, and LL-half loop structure forms. More detailed information is referred to Tian et al.[13,21]. From an engineering application point of view, it was found in previous studies[5,14,17] that as the spanwise coherent vortex structures is destroyed by the formation of vortex dislocations, the magnitude of the structural loads (drag and lift) is decreased.

Although previous studies have widely investigated the flow characteristics of the natural vortex dislocation and the forced vortex dislocation separately, a detailed investigation of the interaction between the natural and forced vortex dislocation is still absent. The primary aim of the present paper is to investigate the flow interactions when the forced and natural vortex dislocations coexist and how such interactions affect the structural loads. To achieve this, the flow past a step cylinder with $D/d$=2 at $Re_D$ =200 (in the mode A$^*$ regime) is studied using a well-validated Direct Numerical Simulation (DNS) code MGLET[22] to directly solve the three-dimensional Navier-Stokes equations.

## II. GOVERNING EQUATIONS, FLOW CONFIGURATION AND COMPUTATIONAL ASPECTS

The incoming flow $U$ is uniform in the positive $x-$direction. The diameter ratio of the step cylinder is given as 2.0. The Reynolds number is $Re_D$=200, based on the diameter of the large cylinder. The origin of the coordinate system is at the step as shown in figures 1. The incompressible flow is governed by the continuity equation and the time-dependent three-dimensional incompressible Navier-Stokes equation:

$$\nabla \cdot \boldsymbol{u} = 0, \tag{1}$$

$$\frac{\partial \boldsymbol{u}}{\partial t} + (\boldsymbol{u} \cdot \nabla)\boldsymbol{u} = \nu \nabla^2 \boldsymbol{u} - \frac{1}{\rho} \nabla p, \tag{2}$$

where $\boldsymbol{u}$ is the velocity vector, while $\rho$, $p$, and $t$ denote the constant density, pressure, and time, respectively.

A finite-volume numerical code MGLET[22] is used to conduct Direct numerical simulations (DNS). This code has been thoroughly validated in previous works for various applications, for example, the flow around step cylinders[13,23], the flow past two tandem cylinders[24,25], and the oscillatory flow through a hexagonal sphere pack[26]. A staggered numerical grid is applied, where the pressure is located in the middle of the grid cell, and the velocities are evaluated in the middle of the grid face. The step cylinder geometry is handled by an immersed boundary method[27,28].

A third-order Runge-Kutta scheme[29] is applied for the time integration. A constant time step $\Delta t$ is used to ensure a CFL (Courant-Friedrichs-Lewy) number smaller than 0.5. Stone's implicit procedure (SIP)[30] is applied to solve the elliptic pressure correction equation.

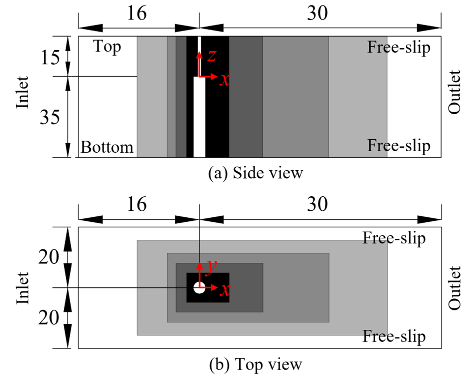


FIG. 2. Computational domain and coordinate system: (a) Side view, (b) Top view. The three directions are named streamwise ($x-$direction), crossflow ($y-$direction) and spanwise ($z-$direction).The grid refinement regions are schematically illustrated and marked with darker shades of grey for finer regions. The length unit is the cylinder diameter $D$.

Figure 2 shows the computational domain and the coordinate system. The inlet and outlet are placed 16$D$ and 30$D$ away from the cylinder axis, respectively. The distance between the top and bottom is 50$D$, where the length of the small and large cylinders is 15$D$ and 35$D$, respectively. The computational domain applied here is comparable to those used in the previous studies[20] for modeling the step cylinder wake at $Re_D$=300. At the inlet, a constant velocity profile ($u$=$U$, $v$=$w$=0) is applied. At the outlet, a Neumann condition ($\partial u/\partial x = \partial v/\partial x = \partial w/\partial x = 0$) is applied. A free-slip boundary condition is applied for the other four sides of the computational domain (for the two vertical sides $v = 0$, $\partial u/\partial y = \partial w/\partial y = 0$; for the two horizontal sides: $w = 0$, $\partial u/\partial z = \partial v/\partial z = 0$). Neumann conditions are applied for the pressure, except at the outlet where the pressure is set equal to zero. A no-slip and impermeability condition ($u = v = w = 0$) is applied on the surface of the step cylinder through an immersed boundary method[27]. Around the cylinder, a local grid refinement is achieved by embedding zonal grids[22]. Figure 2 shows a schematic illustration of the grid design, where the darker shades represent the finer grid regions. The grid is equally sized in the $x-$, $y-$, and $z-$directions within each grid region; the ratio of the grid size between the neighboring regions is equal to two. Two cases with the finest grid resolution 0.0125$D$ (G0125) and 0.01$D$ (G01) have been simulated to conduct a grid convergence study. Table I shows the Strouhal number of the three dominating vortex cells ($St_S = f_S D/U$, $St_N = f_N D/U$, and $St_L = f_L D/U$) behind the step cylinder obtained by a fast Fourier transform (FFT) of the time series of the streamwise velocity $u$ along a vertical sampling line positioned at ($x/D$, $y/D$)=(1.6, 0.4). The differences in $St$ of the same vortex cell between these two cases is small. Figure 3 shows the time-averaged streamwise velocity distribution along the line AB (as indicated in inset (a2)), illustrating the flow variation above the step surface just in front of the small cylinder. The zoom-in view in the inset figure 3(a1) shows that the results from the two cases almost coincide. All flow characteristics and the underpinning mechanisms discussed in the present paper are valid for grid resolutions 0.0125$D$ and 0.01$D$. Moreover, based on the same numerical code MGLET and the same grid resolution 0.01$D$, Jiang et al.[31] obtained novel results in the simulations of flow past a curved cylinder at a higher Reynolds number $Re$ =600. Therefore, we are convinced that the grid resolution 0.01$D$ is sufficiently fine for the present study. The results presented in the following are from the case with the grid resolution 0.01$D$.

TABLE I. Strouhal numbers of the three dominating vortex cells (S-cell, $St_S = f_S D/U$; N-cell, $St_N = f_N D/U$; L-cell, $St_L = f_L D/U$).

| Vortex cell | G0125 | G01 |
|---|---|---|
| $St_S$ | 0.331 | 0.332 |
| $St_N$ | 0.164 | 0.163 |
| $St_L$ | 0.185 | 0.184 |

## III. NATURAL AND FORCED VORTEX DISLOCATIONS

Figure 1(c) shows an overview of the vortex structures in the wake behind the step cylinder with $D/d$=2 at $Re_D$=200 by plotting isosurfaces of $\lambda_2$=-0.05[18]. The three spanwise vortex cells observed in the previous studies[19,20,23] (as shown in figure 1(b)) are also observed in the present study (as shown in figure 1(c)). The corresponding frequency components $St_S = f_s D/U$, $St_N = f_N D/U$, and $St_L = f_L D/U$ for the S-, N-, and L-cell vortices

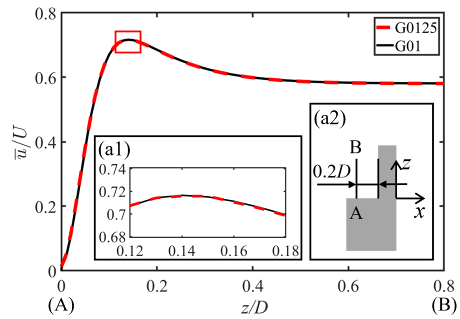


FIG. 3. Distribution of mean streamwise velocity $\overline{u}/U$ along a vertical sampling line AB in the $xz-$plane at $y/D$=0. Insets: (a1) a zoomed-in view of the upper part of the curves (red rectangle); (a2) a sketch of the line AB positioned at $x/D$=-0.45 with a length of 0.8$D$.

are presented in the crossflow velocity spectrum shown in figure 4. Figures 4(a, b) show that the spectrum peak in the N-cell region (-4< $z/D$ <0) and the S-cell region ($z/D$ >0) is more slim and dominating than in the L-cell region ($z/D$ <-4), due to the regular shedding in the S- and N-cell region and the irregular shedding in the L-cell region. The shedding of the S- and N-cell vortices and the interactions between them are similar to that discussed in the step cylinder case at $Re_D$=150[13,21] and $Re_D$=300[20]. The irregular shedding of the L-cell vortex is caused by the coexistence of the forced vortex dislocation (FVD) and natural vortex dislocation (NVD) in the large cylinder wake; the formation of the natural vortex dislocation in the L-cell region changes the shedding frequency in the surrounding region and time interval. Our observations show that, in contrast to the regular formation of FVD between the N- and L-cell vortices in the $Re_D = 150$ and $Re_D = 300$ cases, the coexistence of FVD and NVD in the present $Re_D = 200$ case is found to be able to delay (but not accelerate) the regular formation of FVD under certain circumstances; a detailed discussion will be given below.

Figure 5 shows snapshots of instantaneous vortex structures by plotting isosurfaces of $\lambda_2 = -0.05$. In figures 5(a, b, c), the solid and dashed red curves represent the vortex on the -Y and +Y sides of the step cylinder, respectively. Due to the different dominating shedding frequencies of the N- and L-cell vortices, the forced vortex dislocation occurs periodically between the N- and L-cell vortices at $z/D \approx$-4 around every 48 time units ($D/U$) from $tU/D$=611.1 (figure 5(a)) to $tU/D$=708.1 (figure 5(c)). The L-cell vortex (the red dashed line at -10< $z/D$ <-4) dislocates with its counter N-cell vortex (the red dashed line at -4< $z/D$ <0) on the same cylinder side and

Accepted to Phys. Fluids 10.1063/5.0166526



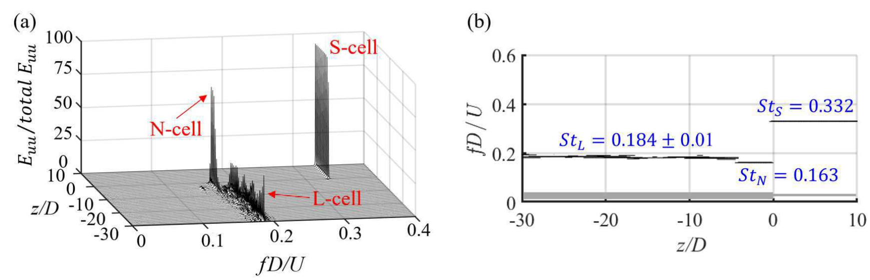


FIG. 4. (a) Streamwise velocity spectra is obtained from a discrete Fourier transform (DFT) of time series of the streamwise velocity $u$ along a vertical sampling line positioned at ($x/D$, $y/D$)=(1.6, 0.4) over 1500 time units ($D/U$) showing the three dominating vortex cells (the S-, N-, and L-cell vortices). (b) Projection of the 3D plot in (a) into the horizontal plane. Only the points with $E_{uu}/(totalE_{uu}) > 7\%$ are shown, indicating the extension and frequency ($St_S$, $St_N$, and $St_L$ for the S-, N-, and L-cell vortices) of the three dominating vortex cells. respectively.

connects to the N-cell (the solid red line at -4< $z/D$ <0) on the other side cylinder side, forming the NL-loop structure. The time interval between these FVDs fits well with the period ($T_{VD} = 1/f_{beat}$) corresponding to the beat frequency[1] ($f_{beat} = f_L - f_N$). Besides the forced vortex dislocation, the one-side and two-side natural vortex dislocation (identified in Tian et al.[32]) is also captured here. In figures 5(a, c, d), the two vortices marked by the solid green lines simultaneously dislocate with the vortex located in-between and marked by the green dashed line, i.e., the two-side NVD. In figures 5(b, c, d), the vortices marked by the solid and dashed blue lines dislocate with each other, i.e., the one-side NVD. Although the formation and position of these two types of NVD are irregular, the regularity of the formation position and period of the FVD from $tU/D$=611.1 to 659.6 shown in figures 5(a, b) is not affected. During this time interval, no NVD occurs in the region $z/D$ >-7, i.e., the region close to the formation position of FVD at $z/D$=-4 (i.e., the NL-boundary). However, this is not always the case. When NVD do occur in the region $z/D > -7$, the formation of the subsequent FVD will be delayed. An example is shown in figure 6: The time interval between the FVDs shown in figures 6(a) and (b) is $80D/U$, which is much larger than that between the FVDs shown in figures 5(b, c, d). From $tU/D$=756.6 (figure 6(a)) to $tU/D$=834.1 (figure 6(b)), a series of NVDs occur at $z/D > -7$; several of them are presented in figures 6(c, d, e). The underpinning mechanism is discussed in the forthcoming. It is worth emphasizing that

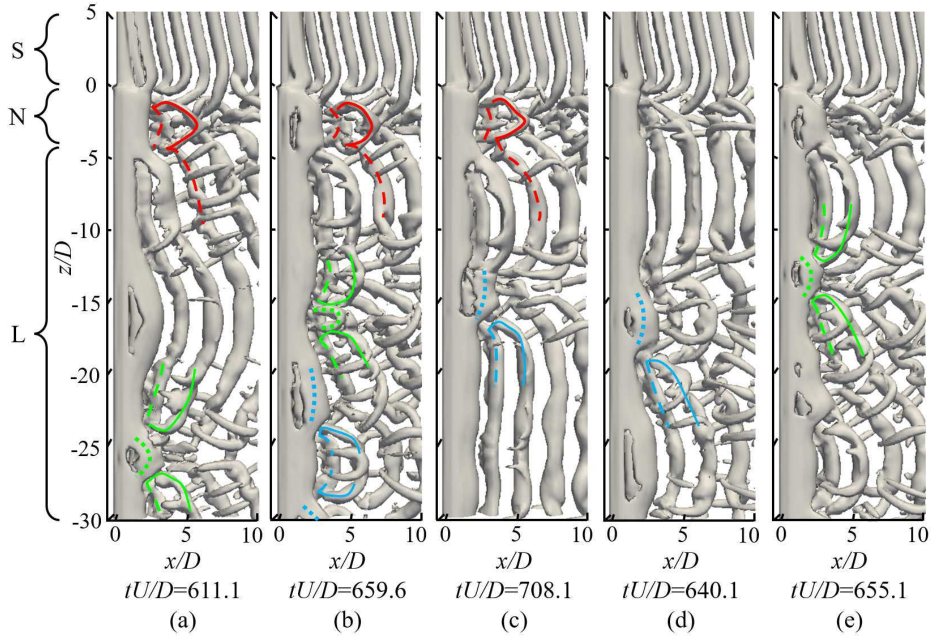


FIG. 5. Isosurfaces of $\lambda_2$=-0.05[18]) illustrating the vortex structures in the wake: (a) $tU/D$=611.1; (b) $tU/D$=659.6; (c) $tU/D$=708.1; (d) $tU/D$=640.1; (e) $tU/D$=655.1. The flow region covered by the three vortex cells (the S-, N-, and L-cell) is shown. The NL-loop vortex structure forms when the forced vortex dislocation occurs between the N- and L-cell vortices; is denoted by the red curve. The blue and green curves indicate the one-side and two-side natural vortex dislocation[32], respectively.

the identification of the formation of FVD and NVD can be achieved by using the number of the neighboring vortices and the formation of the streamwise vortices. The identification will not be affected by the selection of the $\lambda_2$ value. The corresponding detailed information can be found in Tian et al.[13,21,32]. Furthermore, the hand sketches of the vortex structure topology agree well with the vortex rotation axis line obtained by Liutex method[33]. An example is shown in appendix A.

The time history of the shedding frequencies for the regular forced vortex dislocations shown in figures 5(a, b) and the delayed forced vortex dislocations shown in figures 6(a, b) are presented in the left (regular FVD) and right (delayed FVD) column of figure 7. The shedding frequency is estimated from the cross-flow velocity component ($v/U$). Figures 7(a, b) are obtained at the sampling point ($x/D$, $y/D$, $z/D$)=(0.6, 0, -2) which is located in the middle of the N-cell region

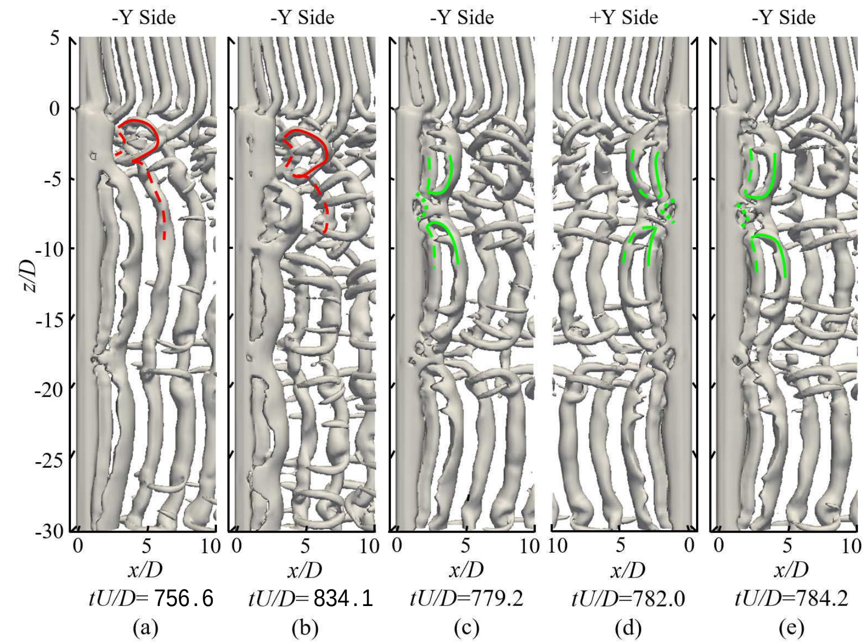


FIG. 6. Isosurfaces of $\lambda_2$=-0.05[18]) illustrating the vortex structures in the wake: : (a) $tU/D$=756.6; (b) $tU/D$=834.1; (c) $tU/D$=779.2; (d) $tU/D$=782.0; (e) $tU/D$=784.2. The same types of curves applied in figure 5 are also used here to denote the forced and natural vortex dislocations.

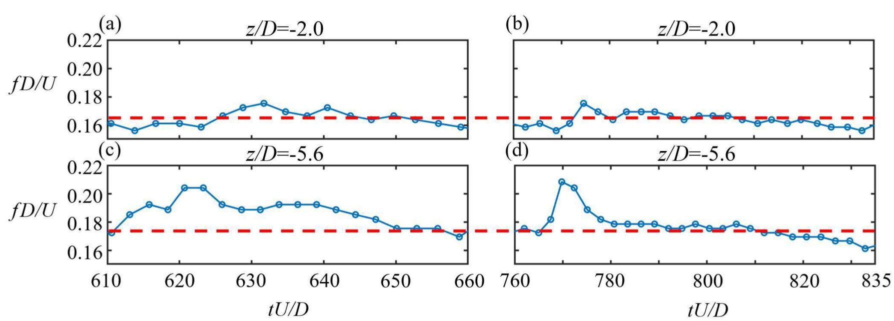


FIG. 7. Time history of the vortex shedding frequency $fD/U$: (a, b) at $z/D$=-2.0 and (c, d) at $z/D$=-5.6; where (a, c) are obtained during the regular forced vortex dislocations shown in figures 5(a, b) and (b, d) are obtained during the delayed forced vortex dislocations shown in figures 6(a, b). The red dashed line is plotted to ease the comparison of the time history between the left and right subplots.

Accepted to Phys. Fluids 10.1063/5.0166526



as shown in figure 5(a), representing the shedding frequency of the N-cell vortex $f_N$. Figures 7(c, d) are obtained at the sampling point ($x/D$, $y/D$, $z/D$)=(0.6, 0, -5.6) which is located in the L-cell region close to the NL-cell boundary and the natural vortex dislocation position as shown in figures 6(b, c, d). This frequency-capture method was also applied in Behara and Mittal[14] and Tian et al.[32]. The time history of the frequency in figures 7(a) and (b) behave similarly, indicating that the shedding frequency in the N-cell region is rarely affected by the natural vortex dislocation. However, the time history of the shedding frequency shown in figure 7(d) is overall lower than that shown in figure 7(c), implying that the shedding frequency of the L-cell vortex at $z/D = -5.6$ clearly decreases during the natural vortex dislocation period. It is known that, in the wake of cylindrical structures, the vortex dislocation (both FVD and NVD) between neighboring spanwise vortices is caused by the accumulation of the phase difference between these vortices[2,13,32]. In the present case, due to the shedding frequency for the N-cell vortex being lower than for the L-cell vortex, the accumulated phase difference between the N- and L-cell vortices will cause FVD to form between them. When $f_N$ and $f_L$ are constant, the period of FVD is constant and equal to $T_{VD} = 1/(f_L - f_N)$. However, as $f_L$ decreases in the region close to the NL-boundary (e.g., $f_L$ shown in figure 7(d)) due to the formation of natural vortex dislocations (e.g., the NVDs shown in figure 6(c, d, e)), the corresponding $T_{VD}$ increases (see the extended time interval between the delayed FVDs shown in figures 6(a, b)). Only the formation of NVD at $z/D > -7$ can affect the

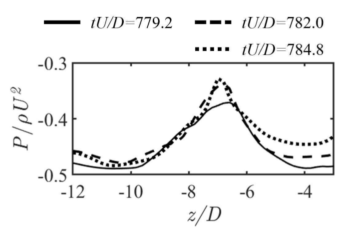


FIG. 8. The spanwise distribution of the instantaneous pressure when NVD occurs at $z/D \approx$-7 in figures 6(c, d, e). The solid and dotted curves are along the sampling line at ($x/D$, $y/D$)=(0.6, -0.2); the dashed curve is at ($x/D$, $y/D$)=(0.6, 0.2).

formation of FVD. This is because the suction pressure decreases locally when NVD occurs. Figure 8 shows the spanwise distribution of the pressure at ($x/D = 0.6$, $y/D = 0.2$) when the natural vortex dislocation occurs in figures 6(c, d, e). It appears that the suction pressure decreases to the local extreme at $z/D$= -7 where two NVDs occur in figures 6(c, d, e); the corresponding affected

Accepted to Phys. Fluids 10.1063/5.0166526



region spans 2–3 diameters ($D$) around the dislocation position. As pointed out in Williamson[1], a decrease in the suction (i.e. an increase in the base pressure) can enlarge the vortex formation region locally and further decrease the vortex shedding frequency; the formation of NVD at a given location can decrease the vortex shedding frequency in a surrounding region covering 4-6 diameters in the spanwise direction. When NVD occurs at $z/D < -7$, it has limited effect on the N- and L-cell vortices around $z/D = -4$ where FVD occurs, i.e., the regular formation of FVD will not be affected.

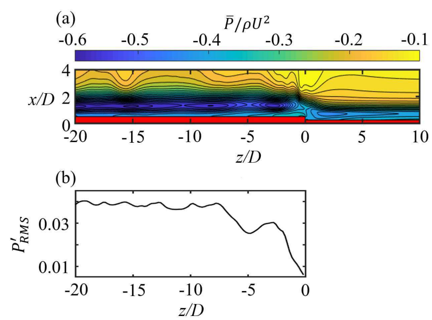


FIG. 9. (a) Time-averaged pressure contour in the $xz-$plane at $y/D$=0. (b) Spanwise distribution of the fluctuated base pressure along the large cylinder at ($x/D$, $y/D$)=(0.6, 0).

As shown in appendix B, long-time observations based on our numerical simulations reveal that NVD can only delay, not accelerate, the formation of FVD in the present case. This is because no natural vortex dislocation forms in the N-cell region (-4<$z/D$<0), i.e., the shedding frequency of the N-cell vortex is not decreased by the formation of the NVD. When only $f_L$ can be decreased due to the NVD, the vortex dislocation period ($T_{VD}$) can only be increased, not decreased, based on the equation $T_{VD} = 1/(f_L - f_N)$. The absence of NVD in the N-cell region could be due to the effect of the weak-suction region behind the small cylinder. Figure 9(a) shows the time-averaged pressure contours in the $xz-$plane at $y/D$=0, indicating that far from the step, the weak-suction region (the yellow region) is located closer to the small cylinder than the large cylinder due to the different diameters. Close to the step ($z/D$=0), the wakes are mixed behind the small and large cylinders. Consequently, the suction pressure in the vicinity of the step decreases on a region behind the large cylinder -4<$z/D$<0 (see figure 9(a)) under the effect of the weak-suction region behind the small cylinder, which also suppresses the flow instability in this region: Figure 9(b) shows the distribution of the root-mean-square of the fluctuating base pressure ($p'_{RMS} = \sqrt{\frac{1}{N}\sum_{i=1}^{N}(p_i - \overline{p})^2}$ where N is the number of values in the sample) along a line behind the large cylinder at ($x/D$, $y/D$)=(0.6, 0), indicating that the value of $p'_{RMS}$ is clearly smaller in the region -4<$z/D$<0 than in the rest of the region along the large cylinder. As the base pressure instability is suppressed, the vortex shedding frequency in the N-cell region becomes more regular than that in the L-cell region (as shown in figure 4), further suppressing the formation of the natural vortex dislocation in the N-cell region -4<$z/D$<0.

In general, the period of the forced vortex dislocations between the slower shedding N-cell vortex and faster shedding L-cell vortex behind a step cylinder is determined by the difference between their shedding frequencies, i.e., $T_{VD} = 1/(f_L - f_N)$. The formation of the forced vortex dislocation is observed to be delayed when NVD occurs at $z/D > -7$ (close to the NL-cell boundary) due to the corresponding decrease of $f_L$. Since the pressure instabilities in the N-cell region are suppressed by the weak suction pressure behind the small cylinder, NVD can not occur in the N-cell region, and thus NVD can only delay, not accelerate, the formation of FVD in the present case. This delay effect has also been observed in flow past a circular cylinder with a downstream sphere (figure 17(b) in Zhao[34]), where the downstream sphere plays a similar role as the small cylinder does in the present case, leading to that NVD can only occur in the region where the faster-shedding vortex is located. It should also be noted that although only the delay effect of NVD on FVD has been observed, we speculate that an acceleration effect of NVD (i.e., a decreases of $T_{VD}$) could exist in other cases where NVD occurs in the region where the slower-shedding vortex is located.

## IV. STRUCTURAL LOAD

Since all interactions between the natural and forced vortex dislocations are located on the large cylinder side of the step cylinder, the present section focuses on how these vortex dislocations affect the structural load of the large cylinder.

Previous studies[5,14,17] have observed that the magnitude of the drag and lift coefficients decrease when vortex dislocations occur in cylinder wakes. Behara and Mittal[5] found that both the mean drag and the amplitude of the lift reach a minimum when the activity of vortex dislocations are at the highest. Figures 10(a, b) show the time history of the drag coefficient $C_D = \frac{2F_D}{\rho U^2 DL}$ (where $F_D$ represents the total drag force on the large cylinder) and the total lift coefficient $C_L = \frac{2F_L}{\rho U^2 DL}$

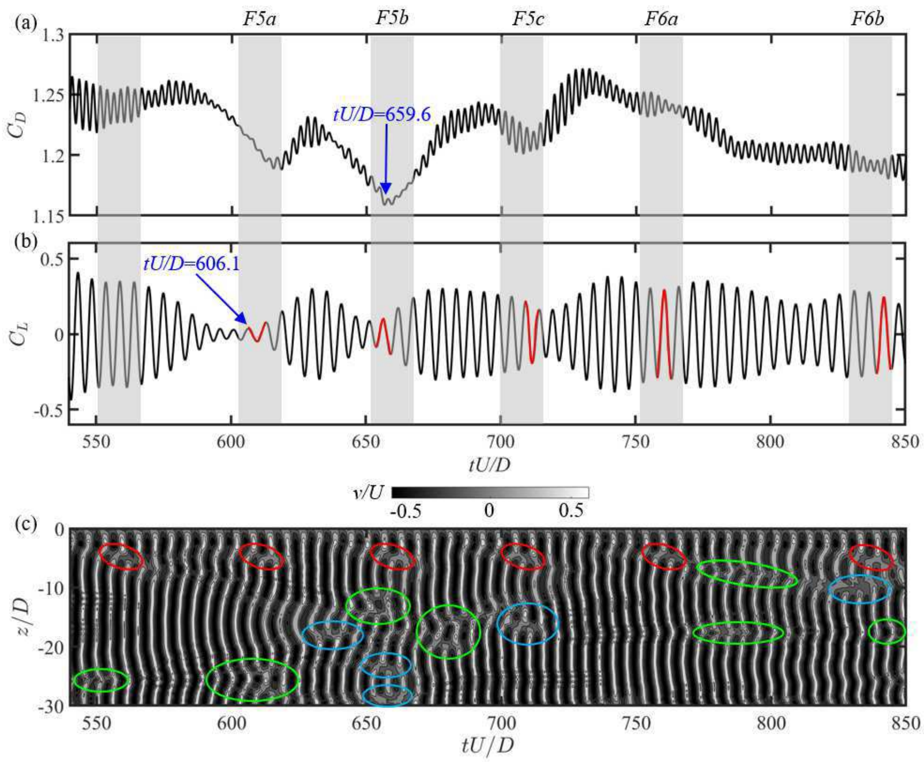


FIG. 10. (a, b) Time history of the drag and lift coefficient on the large cylinder. The time when vortex dislocations occur is highlighted by the transparent rectangles; the one marked by the label $F5a$ corresponds to the dislocation instant shown in figure 5(a). The meaning of the other labels is analogous. (c) Crossflow velocity component $v$ as a function of the non-dimensional time, along spanwise sampling line at $(x/D, y/D)$=(0.6, 0). The red, blue and green circles indicate the occurrence of the forced vortex dislocation, the two-side natural vortex dislocation, and the one-side natural vortex dislocation, respectively.

(where $F_L$ represents the local lift force on the large cylinder). The time instant when vortex dislocations occur is highlighted by the shaded gray rectangles; the one marked by the label $F5a$ is where figure 5(a) is located. Figure 10(c) shows contours of the crossflow velocity $v$, where the occurrence of forced vortex dislocations, two-side natural vortex dislocations, and one-side natural vortex dislocations are indicated by red, blue, and green circles, respectively. The number of spanwise positions where vortex dislocations (natural and forced) occur is shown in table II. Here

TABLE II. Number of spanwise positions where vortex dislocations occur

| Time | F5a | F5b | F5c | F6a | F6b |
|---|---|---|---|---|---|
| Number | 3 | 5 | 3 | 1 | 4 |

one formation of a two-side natural vortex dislocation is treated as two one-side natural vortex dislocations forming simultaneously at two spanwise positions[32]. For example, the two-side natural vortex dislocation sketched by the green curves in figure 5(e) can be treated as two one-side natural vortex dislocation occurring at $z/D \approx$-15 and $z/D \approx$-12. For the other two types of vortex dislocations, it is a one-to-one relation between the number of vortex dislocations and the number of dislocation positions. Figure 10(a) shows that the amplitude of $C_D$ and $C_L$ decreases as vortex dislocations occur. The amplitude of $C_D$ reaches a minimum at $tU/D = 659.6$ (within F5b) when vortex dislocations occur at the largest number of spanwise positions (i.e., when the vortex dislocation activity becomes the highest) compared to the other instants within 550$<tU/D<$850, as indicated in table II and figure 10(c). This is consistent with previous observations[5]. However, the

to the coherence of the spanwise vortex[35], which is affected by the formation of vortex dislocations but is not proportional to the activity of vortex dislocations. To quantify the coherence of the spanwise vortex in the near wake, the spanwise correlation of the crossflow velocity along a spanwise sampling line just behind the large cylinder at ($x/D$, $y/D$)=(0.6, 0) is conducted. The spanwise correlation coefficient of crossflow velocity $v$ between two spanwise positions $z_1$ and $z_2$ is calculated using one vortex shedding period of data by:

$$C_{v12}(z_2) = \frac{\overline{(v(z_1) - \overline{v(z_1)})(v(z_2) - \overline{v(z_2)})}}{\sqrt{\overline{(v(z_1) - \overline{v(z_1)})^2}}\sqrt{\overline{(v(z_2) - \overline{v(z_2)})^2}}}, \qquad (3)$$

where the bar denotes time-averaged taken. The spanwise position where the lift reaches a maximum during the selected period is set up as the reference position ($z_1$) when $C_{v12}$ is calculated within a vortex shedding period. For example, the spanwise distribution of $C_L$ at $tU/D$=606.1 (as

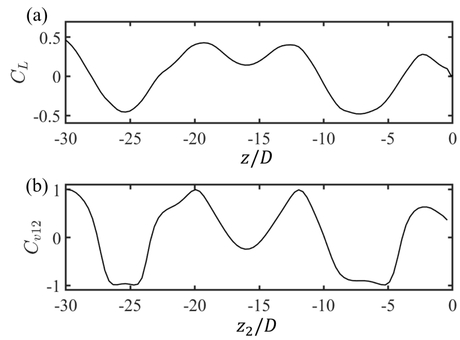


FIG. 11. (a) Spanwise distribution of $C_L$ along the large cylinder at $tU/D$=601 as marked in figure 10(b). (b) Distribution of the correlation coefficient $C_{v12}$ calculated during one vortex shedding period just after $tU/D$=601 with the reference position $z1$=-30.

marked in figure 10(b)) is shown in figure 11(a), showing a maximum at $z/D$ =-30. To study why the amplitude of $C_L$ reaches a minimum at $tU/D$=606.1 in figure 10(b), the correlation coefficient $C_{v12}$ is calculated over the corresponding vortex shedding period (colored in red) with the reference position $z_1$ =-30. The result is shown in figure 11(b). When the coefficient is equal to 1, the vortex structure at the sampling position is completely in-phase with the vortex at the reference potion $z_1$ =-30. This means that the vortex at these two positions shed from the same side of the cylinder simultaneously, contributing to the lift force together. When the coefficient is equal to -1, the vortex at the sampling position is out-of-phase with the vortex at $z/D$ =-30, indicating that the these two vortices (shed from the different sides of the cylinder) cancel each other out and do not contribute to the lift force. Therefore, the coherence of the vortex structure can be evaluated by averaging the correlation coefficient $C_{v12}$ in the spanwise direction. Table III shows $\overline{C_{v12}}$ for five vortex shedding periods within the vortex dislocation duration F5a, F5b, F5c, F6a, and F6b (the corresponding time history of $C_L$ is colored in red in figure 10(b)). First, it is clear that $\overline{C_{v12}}$ and the corresponding amplitude of $C_L$ shown in figure 10(b) behave qualitatively equal. Secondly, a comparison between table II and table III implies that there is no clear relation between the activity of vortex dislocations and the vortex coherence.

Overall, the formation of vortex dislocations cause the amplitude of both the drag $C_D$ and lift $C_L$ coefficient to become smaller, compared to those when no vortex dislocation occurs. The

Accepted to Phys. Fluids 10.1063/5.0166526



amplitude decline of $C_D$ and $C_L$ is dominated by the activity of vortex dislocation and the vortex coherence in the near wake, respectively. The vortex coherence is affected by but not proportional to the activity of vortex dislocation.

TABLE III. Mean correlation coefficient.

| Time | F5a | F5b | F5c | F6a | F6b |
|---|---|---|---|---|---|
| $\overline{C_{v12}}$ | 0.06 | 0.27 | 0.39 | 0.52 | 0.56 |

## V. CONCLUSION

Our present results show good agreement with previous studies, including the three main spanwise vortices[19–21,23], the vortex dislocation mechanism[1,13,17], the vortex dislocation effects in the surrounding flow region[7], and the different topologies of natural vortex dislocations[32]. More importantly, the direct numerical simulations of flow around a single step cylinder with $D/d = 2$ in the mode A* regime ($Re_D = 200$) provide new detailed information about the interaction between the forced vortex dislocation process and the natural vortex dislocation process. The new findings are as follows:

- Since the pressure instabilities in the N-cell region are suppressed by the weak suction pressure behind the small cylinder, natural vortex dislocations can not occur behind the large cylinder close to the step (i.e. the N-cell region $-4 < z/D < 0$). Thus, natural vortex dislocations can only delay, not accelerate, the formation of forced vortex dislocations between the N- and L-cell vortices in the present case by locally decreasing the corresponding shedding frequency of the L-cell vortex.

- The amplitude of both drag ($C_D$) and lift ($C_L$) coefficients decrease when vortex dislocations occur. The activity of vortex dislocations and the vortex coherence in the near wake dominate the amplitude decline of $C_D$ and $C_L$, respectively. The vortex coherence is affected by, but are not proportional to, the activity of vortex dislocation.

## ACKNOWLEDGMENTS

Computing resources were granted by the Norwegian Research Council (Program for Supercomputing) under projects nn9352K and nn9191k.

## CONFLICT OF INTEREST

The author report no conflict of interest.

## DATA AVAILABILITY

The data that support the findings of this study are available from the corresponding author upon reasonable request.

## Appendix A: Topology of vortex

Figure 12(a) shows the isosurface of $\lambda_2$=-0.05 at $tU/D$=659.6, which is directly picked up from figure 5(b). The vortex dislocations are illustrated by the same types of curves as used in figure 5. At the same instant, figure 12(b) shows transparent isosurfaces of $\lambda_2$=-0.05 with vortex rotation axis lines in red calculated based on Liutex method[33]. The zoom-in views of the black rectangles (where the vortex dislocations occur) in figure 12(b) are shown in figures 12(c, d, e). It is clear that the topology of vortex structures indicated by the vortex rotation axis lines in figures 12(c-e) agrees well with that outlined by the hand-sketched curves in figure 12(a).

## Appendix B: Crossflow velocity contour

Figure 13 shows the contour of the crossflow velocity $v$ from $tU/D$=900 to $tU/D$=1500, where the occurrence of forced vortex dislocations, two-side natural vortex dislocations, and one-side natural vortex dislocations are marked by the red, blue, and green circles, respectively. The solid red line marks the spanwise position $z/D$=-7. It appears that the formation of forced vortex dislocations (FVD) can only be delayed when natural vortex dislocations occur in the region above the solid red line (i.e., $z/D > -7$).

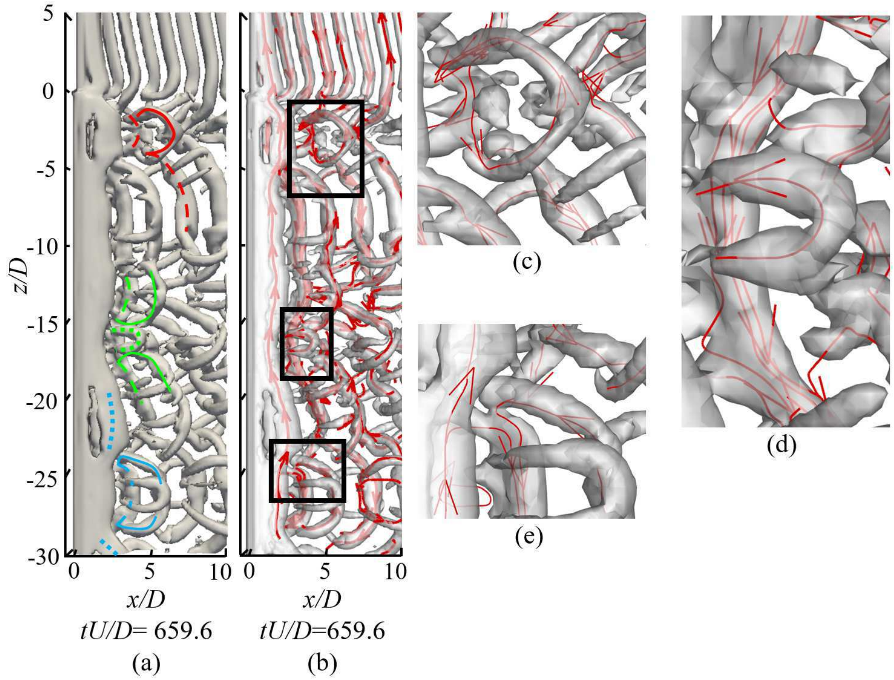


FIG. 12. (a) Isosurfaces of $\lambda_2$=-0.05 illustrating the vortex structure in the wake at $tU/D$=659.6. Directly pick up from figure 5(b). The vortex dislocations are illustrated by the same types of curves as used in figure 5. (b) Transparent isosurfaces of $\lambda_2$=-0.05 at $tU/D$=659.6 with vortex rotation axis lines in red calculated based on Liutex method[33]. (c,d,e) The zoom-in view of the black rectangles in (b).

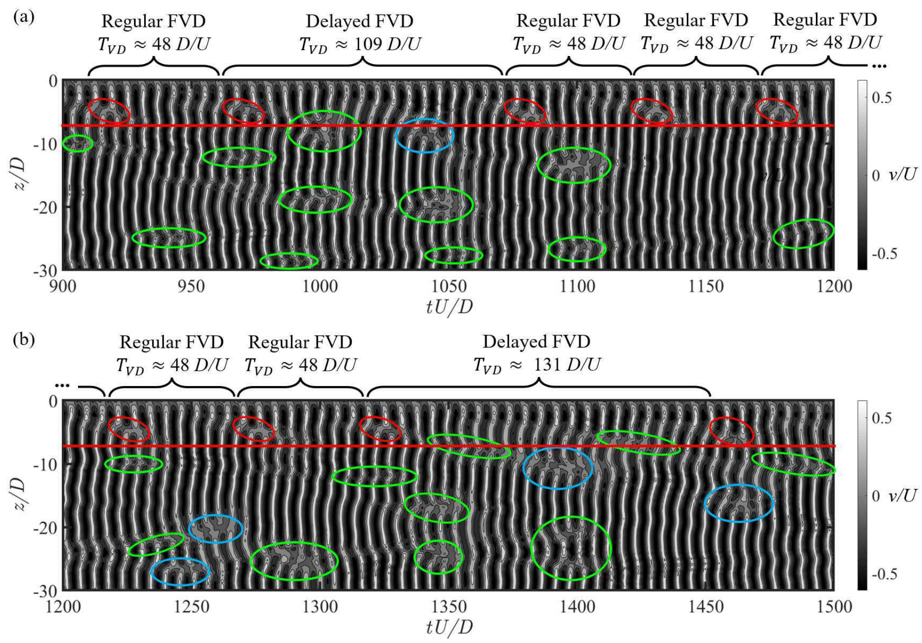


FIG. 13. (a) Crossflow velocity component $v$ as a function of the non-dimensional time, along spanwise sampling line at $(x/D, y/D)$=(0.6, 0) from $tU/D$=900 to $tU/D$=1200. (b) Same as (a) but from $tU/D$=1200 to $tU/D$=1500. The red, blue and green circles indicate the occurrence of the forced vortex dislocation, the two-side natural vortex dislocation, and the one-side natural vortex dislocation, respectively. The spanwise position $z/D = -7$ is marked by the solid red line.

Accepted to Phys. Fluids 10.1063/5.0166526



## REFERENCES

[1] C. H. K. Williamson, "Oblique and parallel modes of vortex shedding in the wake of a circular cylinder at low Reynolds numbers," J. Fluid Mech. **206**, 579–627 (1989).

[2] C. H. K. Williamson, "Three-dimensional wake transition," J. Fluid Mech. **328**, 345–407 (1996).

[3] H. Jiang and L. Cheng, "Transition to chaos in the cylinder wake through the Mode C flow," Phys. Fluids **32**, 014103 (2020).

[4] C. H. K. Williamson, "The natural and forced formation of spot-like 'vortex dislocations' in the transition of a wake," J. Fluid Mech. **243**, 393–441 (1992).

[5] S. Behara and S. Mittal, "Wake transition in flow past a circular cylinder," Phys. Fluids **22**, 114104 (2010).

[6] H. Jiang, L. Cheng, S. Draper, H. An, and F. Tong, "Three-dimensional direct numerical simulation of wake transitions of a circular cylinder," J. Fluid Mech. **801**, 353–391 (2016).

[7] M. Braza, D. Faghani, and H. Persillon, "Successive stages and the role of natural vortex dislocations in three-dimensional wake transition," J. Fluid Mech. **439**, 1–41 (2001).

[8] H. Jiang and L. Cheng, "Strouhal–Reynolds number relationship for flow past a circular cylinder," J. Fluid Mech. **832** (2017).

[9] F. S. Pereira, G. Vaz, L. Eça, and S. S. Girimaji, "Simulation of the flow around a circular cylinder at Re= 3900 with Partially-Averaged Navier-Stokes equations," Int. J. Heat Fluid Flow **69**, 234–246 (2018).

[10] H. Jiang, X. Hu, L. Cheng, and T. Zhou, "Direct numerical simulation of the turbulent kinetic energy and energy dissipation rate in a cylinder wake," Journal of Fluid Mechanics **946**, A11 (2022).

[11] H. Jiang, L. Cheng, F. Tong, S. Draper, and H. An, "Stable state of mode A for flow past a circular cylinder," Phys. Fluids **28**, 104103 (2016).

[12] C. Lewis and M. Gharib, "An exploration of the wake three dimensionalities caused by a local discontinuity in cylinder diameter," Phys. Fluids A-Fluids **4**, 104–117 (1992).

[13] C. Tian, F. Jiang, B. Pettersen, and H. I. Andersson, "Vortex dislocation mechanisms in the near wake of a step cylinder," J. Fluid Mech. **891** (2020).

[14] S. Behara and S. Mittal, "Flow past a circular cylinder at low Reynolds number: Oblique vortex shedding," Phys. Fluids **22**, 054102 (2010).

[15]S. Mittal, J. Pandi, and M. Hore, "Cellular vortex shedding from a cylinder at low Reynolds number," J. Fluid Mech. **915**, A74 (2021).

[16]C. H. K. Williamson, "Vortex dynamics in the cylinder wake," Annu. Rev. Fluid Mech. **28**, 477–539 (1996).

[17]C. Tian, J. Zhu, L. E. Holmeda, H. I. Andersson, F. Jiang, and B. Pettersen, "How vortex dynamics affect the structural load in step cylinder flow," Journal of Fluid Mechanics , 0, A1, (2023).

[18]J. Jeong and F. Hussain, "On the identification of a vortex," J. Fluid Mech. **285**, 69–94 (1995).

[19]W. Dunn and S. Tavoularis, "Experimental studies of vortices shed from cylinders with a step-change in diameter," J. Fluid Mech. **555**, 409–437 (2006).

[20]C. Morton and S. Yarusevych, "Vortex shedding in the wake of a step cylinder," Phys. Fluids **22**, 083602 (2010).

[21]C. Tian, F. Jiang, B. Pettersen, and H. I. Andersson, "Diameter ratio effects in the wake flow of single step cylinders," Phys. Fluids **32**, 093603 (2020).

[22]M. Manhart, "A zonal grid algorithm for DNS of turbulent boundary layers," Comput. Fluids **33**, 435–461 (2004).

[23]C. Tian, F. Jiang, B. Pettersen, and H. I. Andersson, "Vortex system around a step cylinder in a turbulent flow field," Phys. Fluids **33**, 045112 (2021).

[24]T. Aasland, B. Pettersen, H. Andersson, and F. Jiang, "Revisiting the reattachment regime: a closer look at tandem cylinder flow at Re=10000," J. Fluid Mech. **953** (2022).

[25]T. Aasland, B. Pettersen, H. Andersson, and F. Jiang, "Asymmetric cellular bi-stability in the gap between tandem cylinders," J. Fluid Mech. **966**, A39 (2023).

[26]L. Unglehrt and M. Manhart, "Onset of nonlinearity in oscillatory flow through a hexagonal sphere pack," J. Fluid Mech. **944**, A30 (2022).

[27]N. Peller, A. L. Duc, F. Tremblay, and M. Manhart, "High-order stable interpolations for immersed boundary methods," Int. J. Numer. Meth. Fl. **52**, 1175–1193 (2006).

[28]N. Peller, "Numerische simulation turbulenter strömungen mit immersed boundaries," Diss. Universität München (2010).

[29]J. H. Williamson, "Low-storage Runge-Kutta schemes," J. Comput. Phys. **35**, 48–56 (1980).

[30]H. L. Stone, "Iterative solution of implicit approximations of multidimensional partial differential equations," SIAM Journal on Numerical Analysis **5**, 530–558 (1968).

[31]F. Jiang, B. Pettersen, H. Andersson, J. Kim, and S. Kim, "Wake behind a concave curved cylinder," Phys. Rev. Fluids **3**, 094804 (2018).

[32]C. Tian, Z. Shi, F. Jiang, B. Pettersen, and H. I. Andersson, "Different topologies of natural vortex dislocations in mode a wake," Phys. Fluids **34**, 021702 (2022).

[33]C. Liu, Y. Gao, X. Dong, Y. Wang, J. Liu, Y. Zhang, X. Cai, and N. Gui, "Third generation of vortex identification methods: Omega and Liutex/Rortex based systems," J. Hydrodyn. **31**, 205–223 (2019).

[34]M. Zhao, "Flow past a circular cylinder and a downstream sphere for re<300," Journal of Fluid Mechanics **913**, A20 (2021).

[35]C. Norberg, "Fluctuating lift on a circular cylinder: review and new measurements," J. Fluids Struct. **17**, 57–96 (2003).